3D composite reinforcement meso F.E. analyses based on X-ray computed tomography

N. Naouar, E. Vidal-Salle, J. Schneider, E. Maire, P. Boisse

N. Naouar et al./Composite Structures 132 (2015) 1094–1104
http://dx.doi.org/10.1016/j.compstruct.2015.07.005

3D composite reinforcement meso F.E. analyses based on X-ray computed tomography

N. Naouar [a], E. Vidal-Salle [a], J. Schneider [c], E. Maire [b], P. Boisse [a,*]

[a] *Université de Lyon, LaMCoS UMR 5259, INSA-Lyon, 27 av Jean Capelle, F-69621 Villeurbanne, France*
[b] *Université de Lyon, MATEIS UMR 5510, INSA-Lyon, 25 av Jean Capelle, F-69621 Villeurbanne, France*
[c] *SNECMA, Site de Villaroche, Rond Point René Ravaud - Réau, F-77550 Moissy-Cramayel, France*

A B S T R A C T

Meso-FE modelling of 3D textile composites is a powerful tool, which can help determine mechanical properties and permeability of the reinforcements or composites. The quality of the meso FE analyses depends on the quality of the initial model. A direct method based on X-ray tomography imaging is intro- duced to determine finite element models based on the real geometry of 3D composite reinforcements. The method is particularly suitable regarding 3D textile reinforcements for which internal geometries are numerous and complex. The approach used for the separation of the yarns in different directions is specialised because the fibres flow in three-dimensional space. An analysis of the image's texture is per- formed. The homogeneity parameter has proved to be the most efficient criterion to separate the yarns numerically. A hyperelastic model developed for fibre bundles is used for the simulation of the deforma- tion of the 3D reinforcement. Meso-FE simulations based on this approach are performed in the event of transverse compaction of a 3D orthogonal reinforcement. The deformation of the yarns'geometry in the simulation is compared with real conditions.

1. Introduction

A variety of 3D composite reinforcements have been developed to overcome the low delamination fracture toughness of laminated composites. Their common architectural feature is the inclusion of high-stiffness, high-strength fibres in the through-thickness direction [1,2]. These materials help avoid the draping of numerous 2D plies and decrease manufacturing time. These 3D reinforcements are used in different applications, for example in aero engine fan blades [3,4]. Two types of 3D reinforcements can be distinguished. In interlock reinforcements, warp, weft and possible z-binder yarns layers are interlaced during weaving [1,2,5,6]. Another variety of 3D fibre composite is the non-crimp orthogonal woven fabric (Fig. 1). This reinforcement is made by stacking layers of warp and weft yarns linked by orthogonal yarns through the piece's thickness [2,7,8]. Since the warp and weft yarn networks are not interlaced, they avoid crimp. This results in an in-plane stiffness increase when compared with the three-dimensional interlock reinforcement [2,9,10].

At the mesoscopic scale (or meso scale)(Fig. 1) the composite is seen as a set of tows (warp, weft and possible Z-yarn) with or without resin, depending on the type of analysis. When studying periodic structures, mesoscopic models consider the smallest elementary pattern. This repetition unit can reproduce the whole fabric with simple in-plane translations. The repeated structure is called the representative unit cell (RUC) [11–14]. The mesoscopic analyses allow the computation of homogenised composite properties [11,13,15–19], local strains and stresses [13,15,20–23], damage initiation and crack propagation [13,24–26]. During the preforming stage, the deformation analysis of a reinforcement's RUC (with no resin) provides the geometry of the yarns at the resin injection step. The simulation of the resin flow within these deformed tows leads to the computation of the permeability of the reinforcement at different local deformations [27–30]. The reinforcement's mesoscale geometry deformation during manufacturing can also be taken into account in the composite component's mechanical behaviour [31]. One objective of the present paper is the simulation at mesoscale of the large deformations of 3D composite reinforcements as they occur during manufacturing. Deformation of 3D reinforcements has been computed in [32,33] by modelling the yarns as beam elements. The present paper aims to perform 3D F.E. analyses of the 3D reinforcement based on a model obtained from X-ray tomography in order to be as close as possible of the real geometry of the 3D reinforcement.

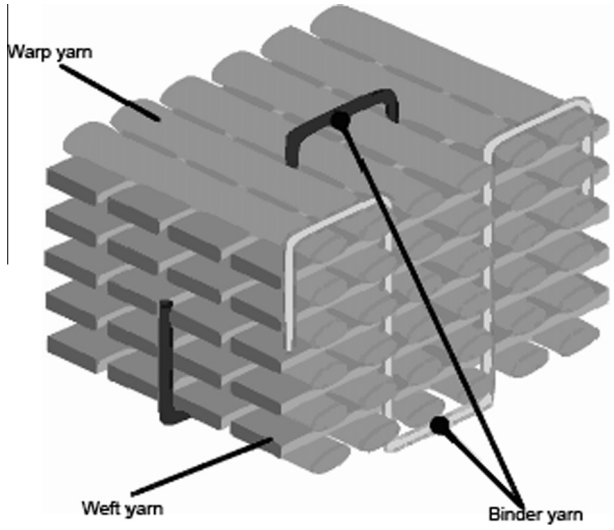

Fig. 1. 3D orthogonal non-crimp woven fibre architecture [2].

The quality of a meso FE analysis strongly depends on the F.E. model, its geometry and the associated data, most important of which being the fibre directions. The geometry can be obtained with textile geometrical simulators such as TexGen or WiseTex [34–37]. Nevertheless, they provide an idealised geometry of the reinforcements which cannot take into account the geometrical imperfections or specificities of the material being analysed. Moreover, reinforcement architectures are diversified and complex for 3D fabrics [1] and all the geometrical possibilities cannot be described by these simulators. In some cases, when the textile reinforcement is thick, and complex, the internal geometry is not completely known. Lastly, interpenetration can occur between the yarns defined by the simulators in some configurations. In the present study, the initial geometry of the meso-FE model of a 3D composite reinforcement is directly obtained from X-ray Micro Tomography (XRMT) also called micro computed tomography (μCT) [38–40]. This fairly recent technique allows for detailed, accurate and non-destructive 3D observations inside a material especially for composites and composite reinforcements [39,41–44]. It distinguishes yarns and even fibres and defines the anisotropic directions of the material. In the present paper, a methodology is used to build automatically finite element models from X-ray micro CT images of 3D composite reinforcements. These models take into account the specificities of the analysed material's geometry. They can be obtained for any reinforcement's weaving style or architecture. A meso FE modelling of a 3D orthogonal non-crimp woven fabric deformation is taken as an example. The segmentation method used is based on the analysis of image texture. For 2D fabrics, the separation of the warp and weft yarns can be obtained by using the structural tensor of the fibre's direction [42]. This is not possible for 3D reinforcements because the fibres flow in three-dimensional space. An approach based on texture analysis for images is used for the 3D composite reinforcement. A method is then submitted to build a prismatic mesh of the yarns. Meso F.E. analysis of the 3D RUC's deformation uses a hyperelastic law for finite strains of fibrous yarns [45]. After a compaction, the internal geometry of the computed and of the experimental 3D reinforcement are compared.

2. Non-crimp 3D orthogonal woven reinforcement

The fabric is an E-glass non-crimp 3D orthogonal woven reinforcement commercialised under trademark HYBON 2001® (by PPG Fibre Glass) (Fig. 2). In Table 1 features of the non-crimp 3D orthogonal weave reinforcement are listed. The 3D fabric has three warp and four weft layers, interlaced with through-thickness yarns in an orthogonal pattern. These images were acquired using a laboratory tomograph Phoenix V tome X, the principles and main functionalities of which are described in [38–41]. The focus, and therefore the resolution, is adjustable from 1 to 5 μm. The detector is made of 1920 × 1575 pixels each with 127 × 127 μm dimensions. Scans performed in this study used beam values close to 90 keV and 170 μA without additional filters. The trade-off between the resolution and the maximum specimen dimension (i.e. yarn width) allows a maximum resolution of 2 μm. The complete sample must be contained within the beam's cone, meaning the field of view of the detector. The uncertainty of the measures made by tomography can be estimated by ±1 voxel. Fig. 2b shows the tomography reconstruction of the Non-crimp 3D orthogonal reinforcement (Fig. 2a) in its non-deformed state.

3. Segmentation

A finite element model is built from tomography images. The pictures extracted from the μCT need to undergo a segmentation process in order to differentiate the wrap, weft and binder yarns. This phase of the process is critical because it impacts the quality of the model significantly. Several segmentation methods are available, one of them, based on the image's structural tensor, seems interesting [42,46,47]. This tensor defines the orientation of fibres in a yarn. This method is efficient if the picture display stringy yarns. It is generally the case for 2D reinforcements. In certain situations, the segmentation based on the orientation tensor cannot be used because the results from the scanning process leads to pictures without stringy yarns but with a grainy aspect. This occurs in 3D reinforcements for images that are perpendicular to or cut the yarns. The present work is based on a Texture Analysis for Image segmentation that is outlined below. This method differentiates 3D reinforcement yarns well.

3.1. Grey level co-occurrence matrix

Texture Analysis for Image Segmentation is based on the calculation of Grey Level Co-occurrence matrix (GLC Matrix) [48]. This method highlights pixel pairs spatially separated by a translation. The generation of co-occurrence matrix is determined by three key points:

- The window size, corresponding to the studied region.
- The number of grey levels (GL) used to describe the image. This number defines the size of the grey level co-occurrence matrix, which is GLxGL. For example, if we take an input image in an 8-bit format, the size of the GLC Matrix will be 256 × 256. In practice, the image is sub-sampled at 16 grey levels.
- The position operator, which is a two-element vector describing the orientation and the distance between the pixel of interest and its neighbour. The conventional orientation is illustrated on Fig. 3 with a distance of one pixel for common angles.

The GLC Matrix calculates how often a pixel with grey-level (greyscale intensity) value *i* occurs horizontally adjacent to a pixel with the value *j*. (We can specify other pixel spatial relationships using the position operator. See Fig. 3.)

Each element (*i, j*) in the GLC Matrix specifies the number of times that the pixel with value *i* occurs horizontally adjacent to a pixel with value *j* in the input image. Fig. 4a shows a matrix that represents an image of size 4 × 4 and contains five grey levels (0–4). Fig. 4b shows the calculated GLC Matrix using the position operator of one horizontally pixel. In the GLC Matrix, element (1,4) contains the value 3 because there are three instances in

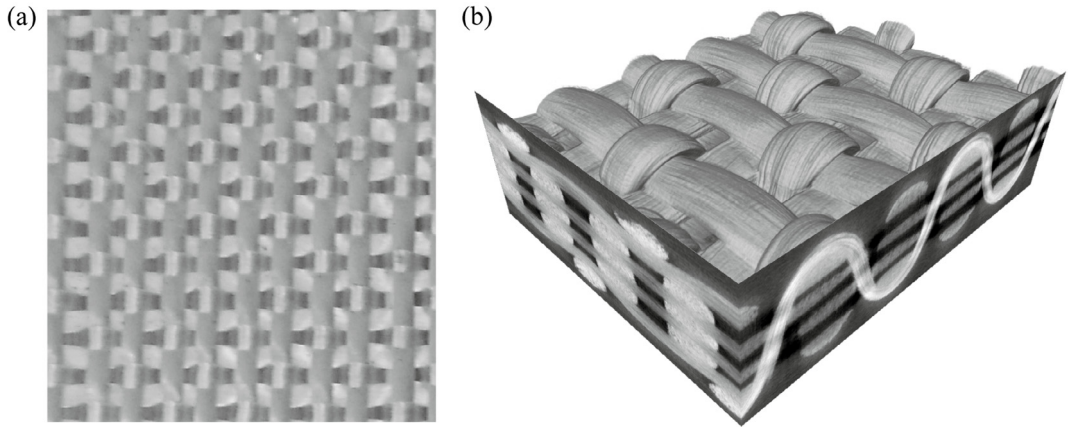

Fig. 2. 3D orthogonal non-crimp woven fabric image (a) and its 3D tomography reconstruction (b).

Table 1
Features of the non-crimp 3D orthogonal weave reinforcement.

Roving Tex (g/km), ±6%	Filament diameter (μm)	Number of filament in a yarn	Areal density (g/m2)	Fabric thickness (mm)
900	15	2000	2722	3.1

the input image where two horizontally adjacent pixels have the values 0 and 3, respectively. Similarly, element (4,5) contains the value 1 because there is only one instance where two horizontally adjacent pixels have the values 3 and 4.

3.2. Statistical analysis

The Grey Level Co-occurrence Matrix contains an important amount of data. However, it cannot be used directly. Hence, fourteen parameters have been defined by Haralick [49] so that textural features can be characterised using the GLC Matrix. The most widely adopted parameters are the contrast, correlation, energy and homogeneity. Once the GLC Matrix is calculated, it is normalised, so that the sum of its components (called $p(i,j)$) is equal to 1. Then, the four statistical parameters (contrast, correlation, energy and homogeneity) are extracted. The contrast parameter (Eq. (1)) returns a measure of the intensity contrast between a pixel and its neighbour in the whole image. This criterion equals 0 for a constant image (that is to say for an image with a constant grey value).

$$Contrast : \sum_{i,j} |i-j|^2 p(i,j) \tag{1}$$

The correlation (Eq. (2)) measures how correlated a pixel is to its neighbour in the whole image. This parameter is between −1 and 1. Parameters μ_i, μ_j, σ_i, et σ_j correspond respectively to the mean and the standard deviation of the pixels in the directions X and Y.

$$Correlation : \sum_{i,j} \frac{(i-\mu_i)(j-\mu_j)p(i,j)}{\sigma_i \sigma_j} \tag{2}$$

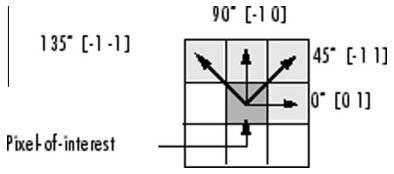

Fig. 3. Position operator convention.

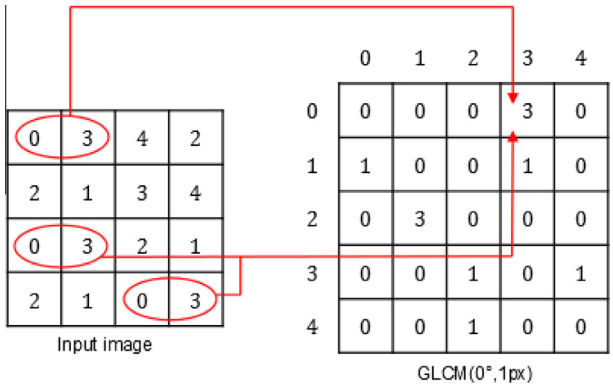

Fig. 4. Example of calculation of the GLC Matrix using a position operator of one horizontally pixel from an input image with five grey levels.

The energy (Eq. (3)) is the sum of the squared GLCM components. It varies between 0 and 1, the value 1 is associated to a constant image.

$$Energy : \sum_{i,j} p(i,j)^2 \tag{3}$$

Finally, homogeneity (Eq. (4)) is a value that measures the closeness of elements' distribution in the GLCM to the GLCM diagonal.

$$Homogeneity : \sum_{i,j} \frac{p(i,j)}{1+|i-j|} \tag{4}$$

3.3. Image processing

In order to distinguish between segment warp and weft yarns, a threshold using the most pertinent parameter is performed. This should result in a concentration of information inside the yarn sections and as few as possible disruptive pixels outside of them.

Homogeneity is the best parameter for extracting yarn sections (Fig. 5d). Contrast (Fig. 5a) and energy (Fig. 5c) separate the yarns as well, however, there is less information inside the sections when compared with the homogeneity method. Moreover, applying a smoothing filter on the parameter can facilitate the threshold. By using a 3D Gaussian filter or a 3D Median filter, it is possible to homogenise the image information: the yarn sections appear more complete. Furthermore, the yarns' cross sections are often not full enough. Additional mathematical morphology operations (closing, convex hull) (Fig. 6) are needed to attain acceptable yarn cross sections and to achieve segmented volume (Fig. 7).

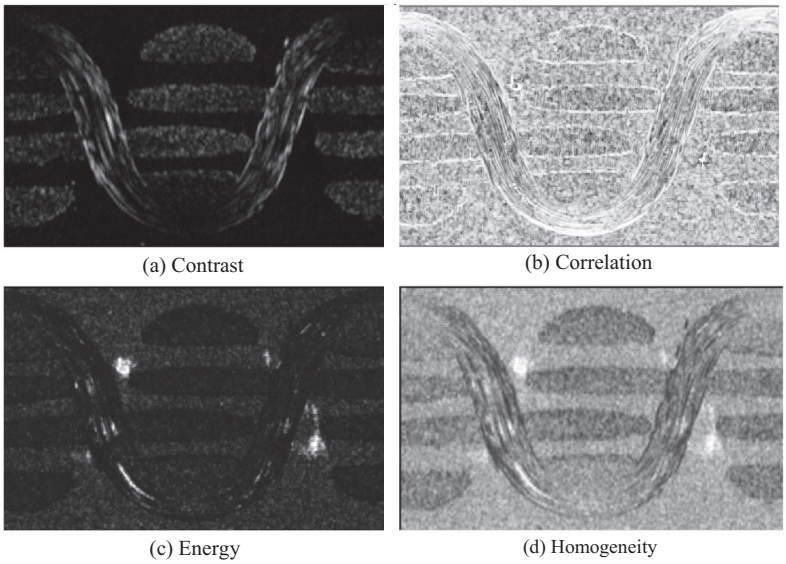

(a) Contrast (b) Correlation

(c) Energy (d) Homogeneity

Fig. 5. GLCM's statistical parameters applied to 3D reinforcement.

4. Mesh generation

4.1. Prismatic finite elements

In meso-scale textile composite modelling, the yarn is considered as a 3D domain. Meshes of the yarn have been generated with hexahedral elements and tetrahedral elements. Nevertheless, neither of these element shapes is completely satisfactory. The hexahedral elements are numerically more efficient and they are well adapted to describe the yarn in the fibre direction [26,45,14,50]. However, it is difficult to mesh the transverse section of the yarn in a suitable manner. Most of the composite yarns have a lenticular shape and, therefore, both extremities are difficult to mesh. On the other hand, the tetrahedral elements can mesh any volume and they efficiently describe the transverse section of the yarn. However, a mesh based on tetrahedrons needs a large number of elements to be sufficiently accurate. In the present work, a prismatic element mesh generator is used. The section is meshed with the triangle edge of the prisms and the quadrangle edges are in the fibre's direction.

4.2. Prismatic mesh generation

First, a transverse section of a yarn is positioned in a regular triangular mesh (larger than the section) (Fig. 8). Only the triangles for which all the nodes are inside the edges of the yarn are retained (in light blue in Fig. 8). An expansion process is then initiated. The edges of the triangles are considered to be springs being compressed ($l = 0.9\ l_0$). The action of the springs lead to triangle expansion. The expansion cannot cross the yarn boundary. After an expansion, the nodes and triangles obtained are optimised by a Delaunay triangulation [51,52] in order to create figures that are as equilateral as possible. The process is repeated until the internal surface of the yarn is completely meshed with triangles optimised by the Delaunay algorithm (Fig. 9).

When a transverse section of a yarn is meshed with triangle elements, wedge elements are obtained by a projection on the next transverse section of the yarn (Fig. 10a). The triangles obtained by this projection must be adjusted in order to match the borders of the new section (Fig. 10b) and in order to be as equilateral as possible (Fig. 10c). The procedure is the same as previously:

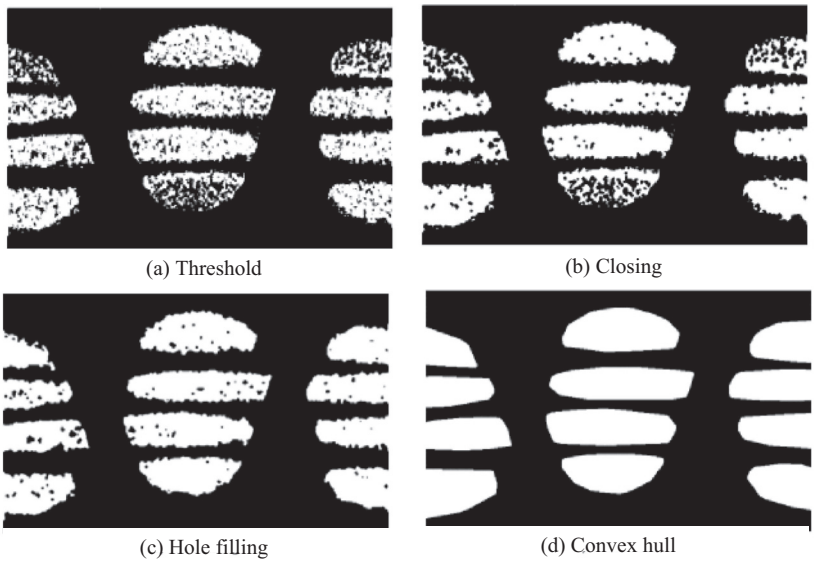

(a) Threshold (b) Closing

(c) Hole filling (d) Convex hull

Fig. 6. Mathematical morphology image processing.

Fig. 7. 3D orthogonal non-crimp segmented volume.

expansion followed by Delaunay triangulation (Fig. 10d). This meshing method is used on the yarns of the 3D orthogonal woven reinforcement (Fig. 11) based on the geometry of the fabric obtained from the μTC analysis (Fig. 7).

4.3. Quality of the prismatic mesh

The objective of this section is to show that the prismatic meshes obtained by the method presented above has a good quality. Numerous studies exist [53,54] on the quality measurement of tetrahedral elements but few concern prismatic elements. The criterion used (Q) in the case of prismatic meshes takes into account three parameters [55]: the aspect ratio R, the maximum of the warping factors w_{max} and the ratio of the W_{max} minimum and maximum Jacobian determinant values (J_{min} and J_{max}). A perfect wedge element is such as Q = 1 and Q = 0 for a flat element.

$$Q = \begin{cases} 0 & J_{min} \leq 0 \\ (1 - R - W_{max})\frac{J_{min}}{J_{max}} & J_{min} > 0 \end{cases} \quad (5)$$

The aspect ratio R is the primary quality measure for a mesh. It is defined as

$$R = \max\left[\frac{\theta_{max} - \theta_e}{180 - \theta_e}, \frac{\theta_e - \theta_{min}}{\theta_e}\right] \quad (6)$$

θ_{max} represents the largest angle in the face, represents the smallest angle in the face, θ_e is equal to 60° for a triangle and 90° for a quadrangle. The ratio determines how close to ideal a face is. (0 for an equilateral face, 1 for a degenerate face). The face aspect ratio is the maximum aspect ratio computed for any face. An ideal wedge is one in which the two triangular faces are equilateral and the three quadrilateral faces are rectangular.

W_{max} is the maximum normalised warping factors. The warping factor W is used to determine if all the four nodes of a quadrilateral face of a wedge are in the same plane [56]. The factor is normalised between 0 and 1, (zero for a perfectly flat face).

J_{min} and J_{max} are the minimum and maximum Jacobian determinants among the nodes of the element. When all the determinants J are equal to each other, the ratio J_{min}/J_{max} has a value of one (wedge with equal length edges).

Finally the range of the proposed metric Q is between [0, 1]. Fig. 12 shows the Q quality criterion for the elements of the yarns of the 3D orthogonal fabric that have been obtained Fig. 11. The quality and uniformity of the mesh is good. All elements are such as Q > 0.7 and the average quality is greater than 0.9. It is often difficult to achieve such a good quality criterion with hexahedral elements in the case of a meso F.E. analysis of a composite reinforcement made of yarns.

5. Constitutive law of the yarn

A hyperelastic constitutive law is used to describe the mechanical behaviour of fibre bundles of woven composite reinforcements at finite strain [45].

5.1. Hyperelastic constitutive equation

The potential energy can be written as a function of the right Cauchy-Green strain tensor $\underline{\underline{C}}$:

$$w = w\left(\underline{\underline{C}}\right) \quad \text{with} \quad \underline{\underline{C}} = \underline{\underline{F}}^T \cdot \underline{\underline{F}} \quad (7)$$

The symmetry group of a transversely isotropic material is characterised, in the initial configuration, by a unit vector $\underline{M}$ which represents the preferred direction. This allows the definition of a

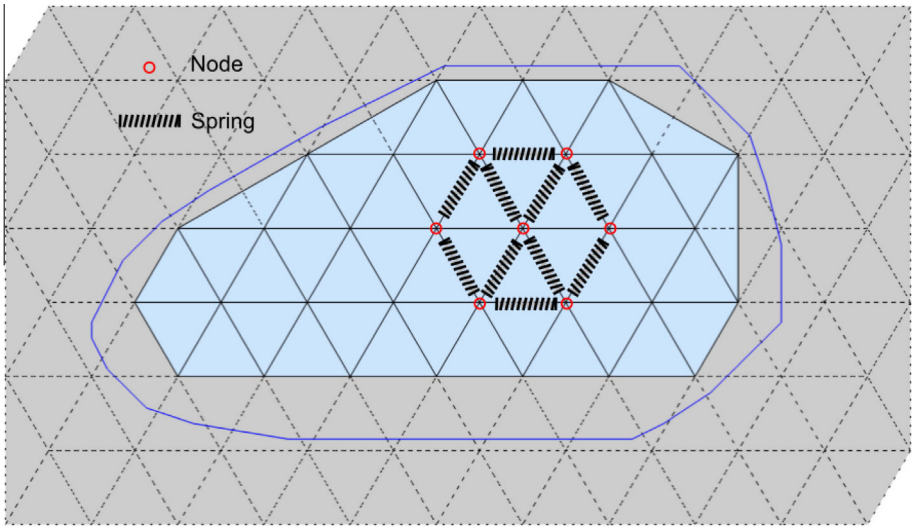

Fig. 8. Initiation of the mesh generation. (For interpretation of the references to colour in this figure legend, the reader is referred to the web version of this article.)

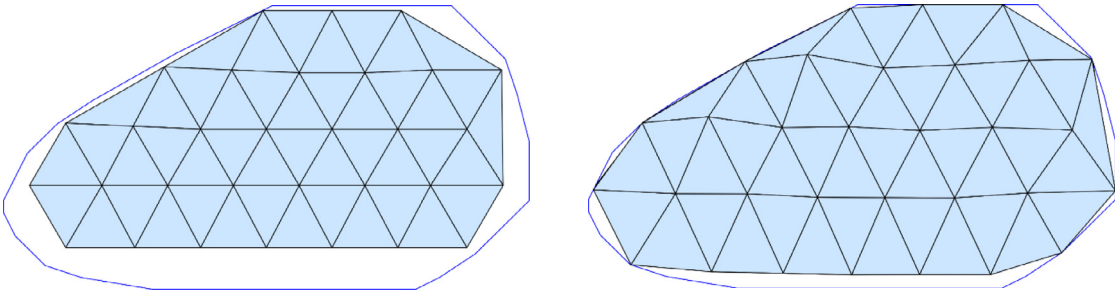

(a) iteration=1

(b) iteration=7

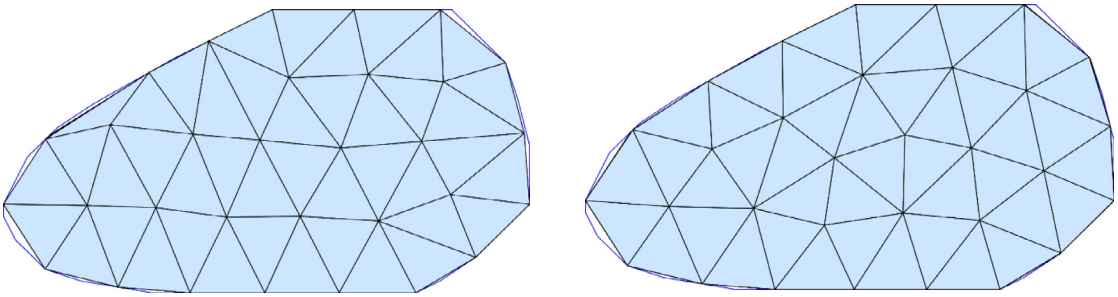

(c) iteration=12

(d) iteration=18

Fig. 9. Surface mesh generation.

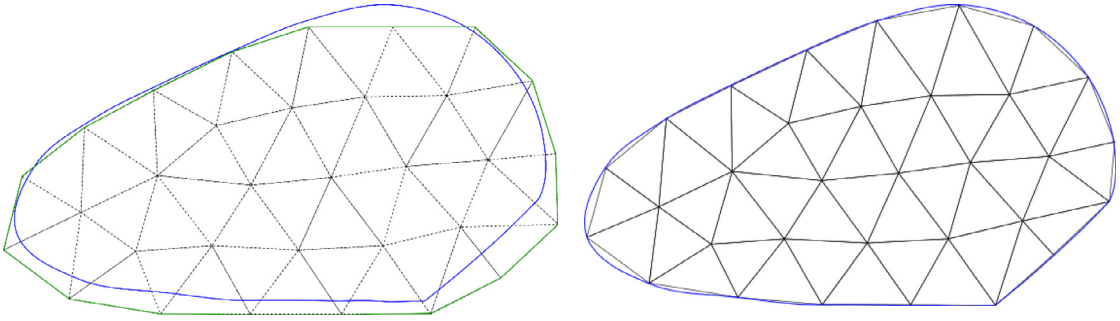

(a) Surface mesh projection

(b) Nodes borders adjustment on the second section

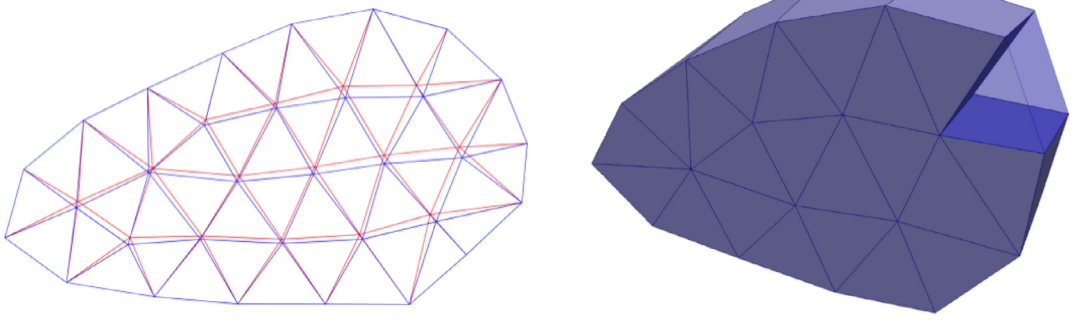

(c) Expansion and Delaunay triangulation

(d) Result of wedge generation between 2 sections

Fig. 10. Generation of wedge mesh.

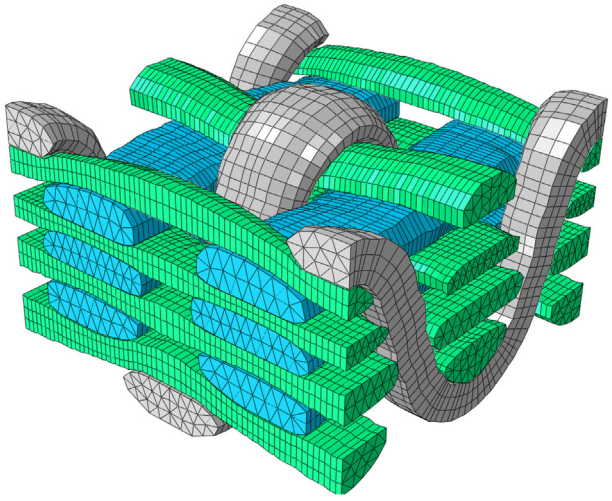

Fig. 11. 3D orthogonal non-crimp woven mesh.

structural tensor $\underline{\underline{M}} = \underline{M} \otimes \underline{M}$. Then, the strain energy potential becomes:

$$w = w(I_1, I_2, I_3, I_4, I_5) \tag{8}$$

where I_1, I_2, I_3 are the invariants of $\underline{\underline{C}}$ defined by:

$$I_1 = Tr\left(\underline{\underline{C}}\right) \quad I_2 = \frac{1}{2}\left(Tr\left(\underline{\underline{C}}\right)^2 - Tr\left(\underline{\underline{C}}^2\right)\right) \quad I_3 = Det\left(\underline{\underline{C}}\right) \tag{9}$$

and where I_4 and I_5 are mixed invariants defined from the structural tensor $\underline{\underline{M}}$ [57]:

$$I_4 = \underline{\underline{C}} : \underline{\underline{M}}, \quad I_5 = \underline{\underline{C}}^2 : \underline{\underline{M}} \tag{10}$$

The contribution of each deformation mode is considered as independent from the others; the second Piola–Kirchhoff stress tensor is then defined as:

$$\underline{\underline{S}} = 2\frac{\partial w}{\partial \underline{\underline{C}}} = \left(\frac{\partial w}{\partial I_1}\frac{\partial I_1}{\partial \underline{\underline{C}}} + \frac{\partial w}{\partial I_2}\frac{\partial I_2}{\partial \underline{\underline{C}}} + \frac{\partial w}{\partial I_3}\frac{\partial I_3}{\partial \underline{\underline{C}}} + \frac{\partial w}{\partial I_4}\frac{\partial I_4}{\partial \underline{\underline{C}}} + \frac{\partial w}{\partial I_5}\frac{\partial I_5}{\partial \underline{\underline{C}}}\right). \tag{11}$$

5.2. Physically based invariants

The behaviour law is based on the physics of the tow deformation [45]. Four deformation modes can be identified (Fig. 13): elongation in the fibre direction, compaction in the transverse section of the yarn, distortion (shear) in the transverse section and shear along the fibre direction. The last mode (longitudinal shear) mainly controls the bending rigidity of the yarn. It is a compound of two equivalent deformation modes corresponding to the two directions of shear. The following set of invariants, corresponding to these four deformation modes, is defined in function of the classical invariants I_1 to I_5 defined above:

$$I_{elong} = \frac{1}{2}\ln(I_4) \quad I_{comp} = \frac{1}{4}\ln\left(\frac{I_3}{I_4}\right) \tag{12}$$

$$I_{dist} = \frac{1}{2}\ln\left(\frac{I_1 I_4 - I_5}{2\sqrt{I_3 I_4}} + \sqrt{\left(\frac{I_1 I_4 - I_5}{2\sqrt{I_3 I_4}}\right)^2 - 1}\right) \quad I_{sh} = \sqrt{\frac{I_5}{I_4^2} - 1} \tag{13}$$

These invariants are used to define the strain energy functions associated to each deformation mode:

$$w\left(\underline{\underline{C}}\right) = w(I_{elong}, I_{comp}, I_{dist}, I_{sh}) \tag{14}$$

The elongation strain energy potential is defined piecewise: a nonlinear part w^{nl}_{elong} when $I_{elong} \le I^0_{elong}$ and a linear one w^{lin}_{elong} when $I_{elong} > I^0_{elong}$. Introducing the initial yarn section S_0, its initial stiffnesses K^0_{elong}, its stiffness in its linear part K_{elong}, and the continuity condition between the two functions w^{nl}_{elong} and w^{lin}_{elong}, leads to:

$$w^{nl}_{elong} = \frac{K^0_{elong}}{2S_0} I^2_{elong} + \frac{K_{elong} - K^0_{elong}}{6S_0 I^0_{elong}} I^3_{elong} \tag{15}$$

$$w^{lin}_{elong} = \frac{K_{elong} - K^0_{elong}}{6S_0}\left(I^0_{elong}\right)^2 - \frac{K_{elong} - K^0_{elong}}{2S_0} I^0_{elong} I_{elong} + \frac{K_{elong}}{2S_0} I^2_{elong} \tag{16}$$

The strain energy associated to the transverse compaction of the yarn is linked to several physical phenomena at the microscopic

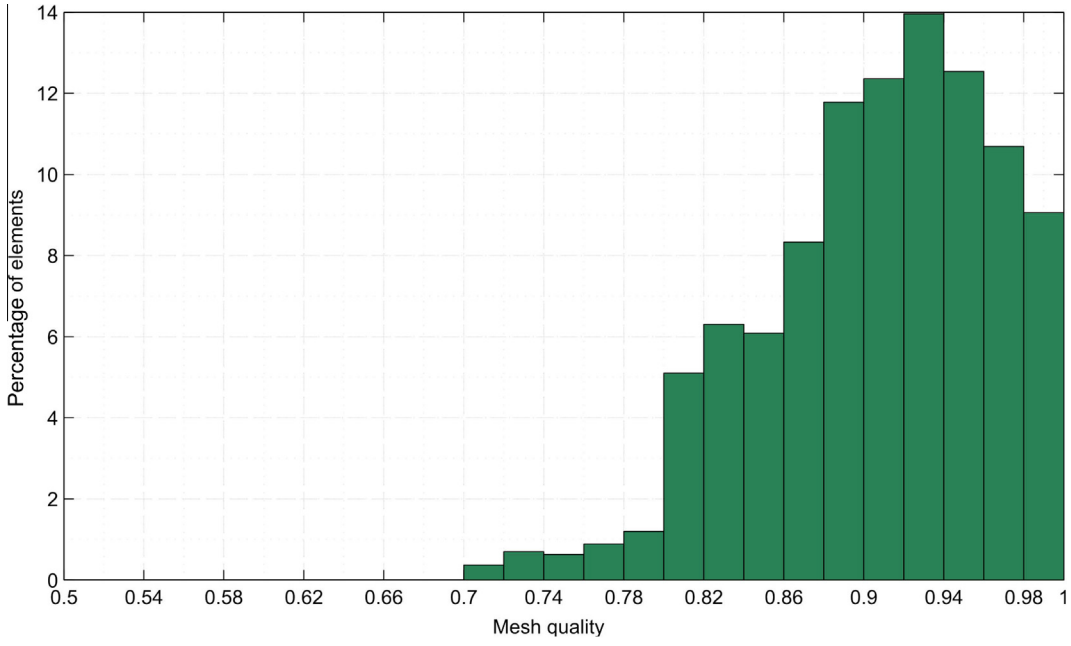

Fig. 12. Distribution of the number of elements depending on the quality for the mesh of the 3D orthogonal fabric.

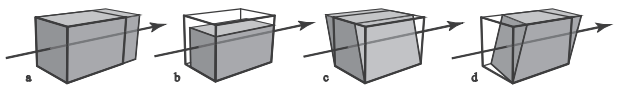

Fig. 13. Deformation modes of the yarn: (a) elongation, (b) compaction of the cross section, (c) distortion of the cross section and (d) longitudinal shear. The arrow indicates the direction of fibres.

Table 2
Parameters of the hyperelastic law.

S_0 (mm)	I^0_{elong}	K^0_{elong} (N)	K_{elong} (N)	K^0_{sh} (MPa)	K^0_{comp} (N)	P	K_{dist} (MPa)
0.489	0.0038626	11,000	37,486	3	17,812	7.72	0.06

scale (mostly bending and rearrangement of fibres) which are difficult to study separately. As in [45,58], a power-based strain energy function is used:

$$w_{comp}(I_{comp}) = \begin{vmatrix} K_{comp}|I_{comp}|^p & \text{if} \quad I_{comp} \le 0 \\ 0 & \text{if} \quad I_{comp} > 0 \end{vmatrix} \tag{17}$$

It is assumed that no energy is required for yarn section expansion. During the formation of a textile composite reinforcement, yarn compaction stiffness is considered to never reach the bulk stiffness of glass (i.e. the voids in the yarn do not collapse altogether).

The distortion strain energy is assumed to be in the form:

$$w_{dist}(I_{dist}) = \frac{1}{2}K_{dist}I^2_{dist} \tag{18}$$

The longitudinal shear strain energy of the yarn is linked to the sliding of its constitutive fibres in their preferred direction. A linear elastic behaviour will be presumed for this deformation mode, which induces the following strain energy potential:

$$w_{sh}(I_{sh}) = \frac{1}{2}K_{sh}I^2_{sh} \tag{19}$$

Finally, the whole constitutive equation is the summation of all contributions discussed above:

$$\begin{aligned} \underline{\underline{S}} &= 2\left(\frac{\partial w_{elong}}{\partial I_{elong}}\frac{\partial I_{elong}}{\partial \underline{\underline{C}}} + \frac{\partial w_{comp}}{\partial I_{comp}}\frac{\partial I_{comp}}{\partial \underline{\underline{C}}} + \frac{\partial w_{dist}}{\partial I_{dist}}\frac{\partial I_{dist}}{\partial \underline{\underline{C}}} + \frac{\partial w_{sh}}{\partial I_{sh}}\frac{\partial I_{sh}}{\partial \underline{\underline{C}}}\right) \\ &= \underline{\underline{S}}_{elong} + \underline{\underline{S}}_{comp} + \underline{\underline{S}}_{dist} + \underline{\underline{S}}_{sh} \end{aligned} \tag{20}$$

The constitutive law depends on eight parameters: four corresponding to longitudinal elongation, two to yarn compaction, one

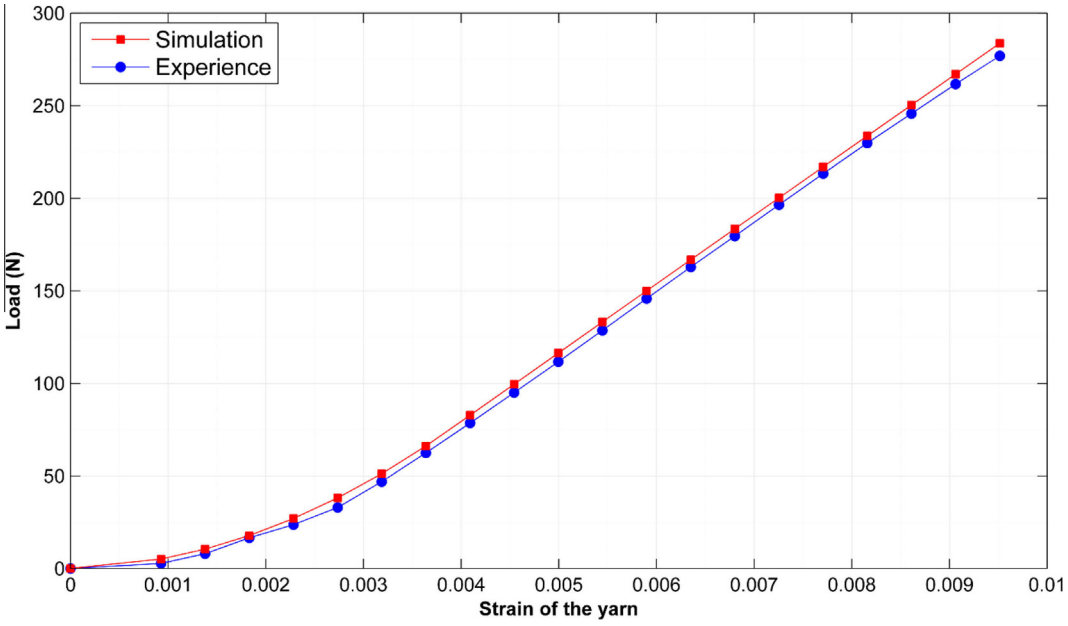

Fig. 14. Identification of yarn elongation behaviour.

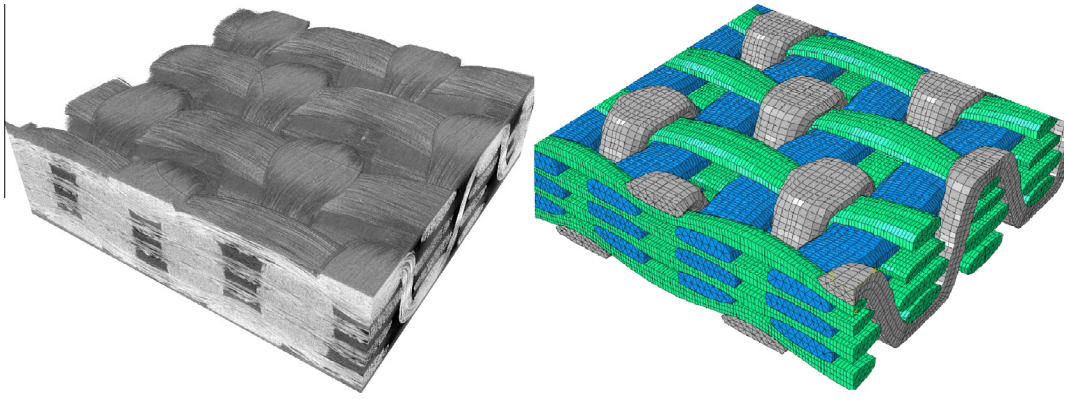

Fig. 15. Comparison between the compacted tomography and the 3D orthogonal non-crimp woven simulation.

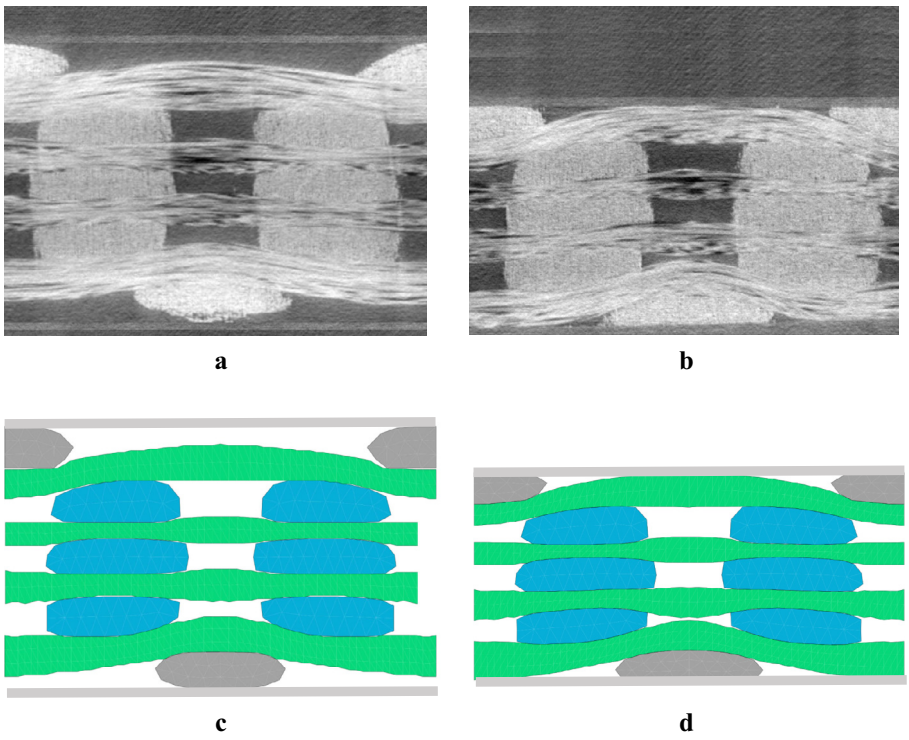

Fig. 16. 3D orthogonal non-crimp woven compaction (a,c) initial state. (b,d) after a 22% compaction.

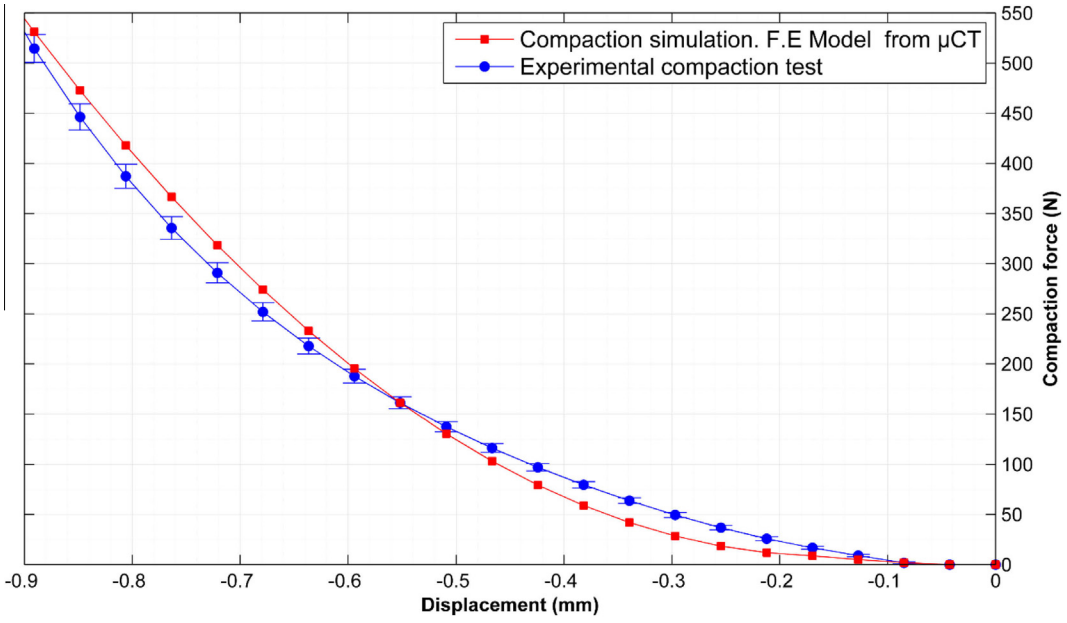

Fig. 17. Comparison between simulated and tomographied 3D orthogonal non-crimp woven compacted to 22%.

to yarn distortion and one to longitudinal shear. This constitutive equation has been implemented as a user material subroutine VUMAT in the ABAQUS/Explicit finite element code.

5.3. Meso-scale F.E. simulations

Meso-scale F.E. simulations of transverse compaction are performed on the 900 Tex fabric. The material parameters are displayed in Table 2. The initial section of the yarn, S_0, is determined by mesoscale observations of the fabric, using X-ray tomography for instance. The three other parameters, namely I^0_{elong}, K^0_{elong} and K_{elong}, are identified with a tensile test on a single yarn. Since the yarn may have been damaged during weaving, this test must be performed on a yarn extracted from the fabric rather than before weaving. The parameters obtained by this method for the glass fibre yarn, as well as the experimental and identified curves, are shown on Fig. 14. The others parameters come from [45]. Fig. 15 shows geometries obtained by tomography and

simulation of the 3D reinforcement submitted to a transverse compaction. The reinforcement was compacted to 22% of its original length between two plexiglass plates linked by four screws. The compaction of the binder yarn obtained in the simulation is consistent with tomography. Transverse sections of the initial and deformed geometries (from tomography and from the simulation) are compared on Fig. 16. The computed deformed geometry is in agreement with the geometry obtained from tomography. Fig. 17 shows the comparison between the experimental and computed compaction loads (loads on the compression machine). These loads are coherent.

6. Conclusions

X-ray tomography is well adapted to the development of 3D textile composite meso-FE models directly from reinforcement specimens. The complexity of their geometry and of the yarn interlacing can be taken into account with μCT images. A segmentation method based on image texture has been explored to separate the warp, weft and binder yarns in the μCT images. This approach is better adapted to the study than a structure tensor approach commonly used for 2D fabrics because the yarns are oriented in all directions of space. The yarns are meshed by prism finite elements. This shape is well suited to fibrous yarn geometry. The triangle edges mesh the transverse section of the tows. Meso-F.E. analyses have been performed using a hyperelastic model developed previously for fibre bundles. This constitutive law is well adapted to these simulations. The comparisons between experimental trials and the computed internal deformed geometry have shown coherent results. This method must now be applied in other cases in order to check its robustness. Moreover, the meso-FE is used in the computation of 3D reinforcement permeability. The composite reinforcement is compacted and/or sheared before the resin injection phase of the R.T.M process. The internal geometry after compaction or shearing can be used to perform flow analyses and determine the permeability properties.

Acknowledgements

The collaboration with SNECMA is gratefully acknowledged. This work was supported under by PRC Composites. Research project funded by DGAC, involving SAFRAN Group, ONERA and the CNRS.

References

[1] Mouritz AP. Three-dimensional (3D) fibre reinforcements for composites. In: Boisse P, editor. Composite reinforcements for optimum performance. Woodhead Publishing; 2011. p. 157–99.
[2] Mouritz A, Bannister M, Falzon P, Leong K. Review of applications for advanced three-dimensional fibre textile composites. Compos A Appl Sci Manuf 1999;30(12):1445–61.
[3] de Luycker E, Morestin F, Boisse P, Marsal D. Simulation of 3D interlock composite preforming. Compos Struct 2009;88(4):615–23.
[4] Gras R, Leclerc H, Hild F, Roux S, Schneider J. Identification of a set of macroscopic elastic parameters in a 3D woven composite: uncertainty analysis and regularization. Int J Solids Struct 2015;55:2–16.
[5] Legrand X, Boussu F, Nauman S, Cristian I, Lapeyronnie P, Grognec PL, et al. Forming behaviour of warp interlock composite. Int J Mater Form 2009;2:177–80.
[6] Dufour C, Wang P, Boussu F, Soulat D. Experimental investigation about stamping behaviour of 3D warp interlock composite preforms. Appl Compos Mater 2013;21:725–38.
[7] Carvelli V, Pazmino J, Lomov S, Verpoest I. Deformability of a non-crimp 3D orthogonal weave E-glass composite reinforcement. Compos Sci Technol 2012;73:9–18.
[8] Pazmino J, Carvelli V, Lomov SV. Micro-CT analysis of the internal deformed geometry of a non-crimp 3D orthogonal weave E-glass composite reinforcement. Compos B Eng 2014;65:147–57.
[9] Mohamed M, Zhang Z, Dickinson L. Manufacture of multilayer woven preforms. Adv Compos Proc Technol 1988;5:81–90.
[10] Ansar M, Xinwei W, Chouwei Z. Modeling strategies of 3D woven composites: a review. Compos Struct 2011;93(8):1947–63.
[11] Tang XD, Whitcomb JD. General techniques for exploiting periodicity and symmetries in micromechanics analysis of textile composites. J Compos Mater 2003;37(13):1167–89.
[12] Miehe C, Dettmar J. A framework for micro–macro transitions in periodic particle aggregates of granular materials. Comput Methods Appl Mech Eng 2004;193(3):225–56.
[13] Lomov SV, Ivanov DS, Verpoest I, Zako M, Kurashiki T, Nakai H, et al. Meso-FE modelling of textile composites: road map and data flow and algorithms. Compos Sci Technol 2007;67(9):1870–91.
[14] Badel P, Vidal-Salle E, Boisse P. Computational determination of in-plane shear mechanical behaviour of textile composite reinforcements. Comput Mater Sci 2007;40(4):439–48.
[15] Peng X, Cao J. A dual homogenization and finite element approach for material characterization of textile composites. Compos B 2002;33(45):56.
[16] Le Corre S, Caillerie D, Orgeas L, Favier D. Behavior of a net of fibers linked by viscous interactions: theory and mechanical properties. J Mech Phys Solids 2004;52:395–421.
[17] Lapeyronnie P, Grognec PL, Binetruy C, Boussu F. Homogenization of the elastic behavior of a layer-to-layer angle-interlock composite. Compos Struct 2011;93:2795–807.
[18] Chaouachi F, Rahali Y, Ganghoffer JF. A micromechanical model of woven structures accounting for yarn-yarn contact based on Hertz theory and energy minimization. Compos B Eng 2014;66:368–80.
[19] Syerko E, Comas-Cardona S, Binetruy C. Models for shear properties/behavior of dry fibrous materials at various scales: a review. Int J Mater Form 2015;8:1–23.
[20] Allaoui S, Hivet G, Wendling A, Ouagne P, Soulat D. Influence of the dry woven fabrics meso-structure on fabric/fabric contact behavior. J Compos Mater 2012;46:627–39.
[21] Gereke T, Döbrich O, Hübner M, Cherif C. Experimental and computational composite textile reinforcement forming: a review. Compos Part A 2013;46:1–10.
[22] Stier B, Doitrand, Simon JW, Reese S. Comparing experimental results to a numerical meso-scale approach for woven fiber reinforced plastics. Compos Struct 2015;122:553–60.
[23] Smerdova O, Sutcliffe MPF. Multiscale tool–fabric contact observation and analysis for composite fabric forming. Compos A 2015;73:116–24.
[24] Pickett AK, Fouinneteau MRC. Material characterisation and calibration of a meso-mechanical damage model for braid reinforced composites. Compos A Appl Sci Manuf 2006;37(2):368–77.
[25] Lemanski SL, Wang J, Sutcliffe MPF, Potter KD, Wisnom MR. Modelling failure of composite specimens with defects under compression loading. Compos A 2013;48:26–36.
[26] Obert E, Daghia F, Ladeveze P, Ballere L. Micro and meso modeling of woven composites: transverse cracking kinetics and homogenization. Compos Struct 2014;117:212–21.
[27] Bickerton S, Simacek P, Guglielmi SE, Advani SG. Investigation of draping and its effects on the mold filling process during manufacturing of a compound curved composite part. Compos A Appl Sci Manuf 1997;28(9–10):801–16.
[28] Loix F, Badel P, Orgeas L, Geindreau C, Boisse P. Woven fabric permeability: from textile deformation to fluid flow mesoscale simulations. Compos Sci Technol 2008;68(7–8):1624–30.
[29] Tran T, Comas-Cardona S, Abriak NE, Binetruy C. Unified microporomechanical approach for mechanical behavior and permeability of misaligned unidirectional fiber reinforcement. Compos Sci Technol 2010;70:1410–8.
[30] Zeng X, Endruweit A, Brown L, Long A. Numerical prediction of in-plane permeability for multilayer woven fabrics with manufacture-induced deformation. Compos A 2015. http://dx.doi.org/10.1016/j.compositesa.2015.03.027.
[31] Mahdi S, Gama BA, Yarlagadda Jr S. Effect of the manufacturing process on the interfacial properties and structural performance of multi-functional composite structures. Compos A Appl Sci Manuf 2003;34(7):635–47. JWG.
[32] Green SD, Long AC, El Said BSF, Hallett SR. Numerical modelling of 3D woven preform deformations. Compos Struct 2014;108:747–56.
[33] Green SD, Matveev MY, Long AC, Ivanov D, Hallett SR. Numerical modelling of 3D woven preform deformations. Compos Struct 2014;108:747–56.
[34] Lin H, Zeng X, Sherburn M, Long AC, Clifford MJ. Automated geometric modelling of textile structures. Text Res J 2012;82:1689–702.
[35] Long AC, Brown LP. Modelling the geometry of textile reinforcements for composites: TexGen. In: Boisse P, editor. Composite reinforcements for optimum performance. Woodhead Publishing; 2011. p. 239–64.
[36] Lomov SV. Modelling the geometry of textile reinforcements for composites: WiseTex. In: Boisse P, editor. Composite reinforcements for optimum performance. Woodhead Publishing; 2011. p. 200–38.
[37] Wendling A, Daniel JL, Hivet G, Vidal-Salle E, Boisse P. Meshing preprocessor for the mesoscopic 3D finite element simulation of 2D and interlock fabric deformation. Appl Compos Mater 2015:1–18. http://dx.doi.org/10.1007/s10443-015-9441-8.
[38] Baruchel J, Buffiere JY, Maire E, Merle P, Peix G. X-Ray Tomography in Material Science. In: Baruchel J, Buffiere JY, Maire E, Merle P, Peix G, editors. Hermes Science.
[39] Desplentere F, Lomov SV, Woerdeman DL, Verpoest I, Wevers M, Bogdanovich A. Micro-CT characterization of variability in 3D textile architecture. Compos Sci Technol 2005;65(13):1920–30.

[40] Hsieh J. In: Hsieh J, editor. Computed tomography: principles, design, artifacts, and recent advances. SPIE Press; 2009.
[41] Jeon SY, Na WJ, Choi YO, Lee MG, Kim HE, Yu WR. In situ monitoring of structural changes in nonwoven mats under tensile loading using X-ray computer tomography. Compos A 2014;63:1–9.
[42] Naouar N, Vidal-Salle E, Schneider J, Maire E, Boisse P. Meso-scale FE analyses of textile composite reinforcement deformation based on X-Ray computed tomography. Compos Struct 2014;116:165–76.
[43] Straumit I, Lomov SV, Wevers M. Quantification of the internal structure and automatic generation of voxel models of textile composites from X-ray computed tomography. Compos A 2015;69:150–8.
[44] Barburski M, Straumit I, Zhang X, Wevers M, Lomov SV. Micro-CT analysis of internal structure of sheared textile composite reinforcement. Compos A Appl Sci Manuf 2015;73:45–54.
[45] Charmetant A, Vidal-Salle E, Boisse P. Hyperelastic modelling for mesoscopic analyses of composite reinforcements. Compos Sci Technol 2011;71(14): 1623–31.
[46] Rezakhaniha R, Agianniotis A, Schrauwen JTC, Griffa A, Sage D, Bouten CVC, et al. Experimental investigation of collagen waviness and orientation in the arterial adventitia using confocal laser scanning microscopy. Biomech Model Mechanobiol 2011;11(3–4):461–73.
[47] Jeulin D, Moreaud M. Segmentation of 2D and 3D textures from estimates of the local orientation. Image Anal Stereology 2008;27:183–92.
[48] Haralick RM, Shapiro LG. Computer and robot vision. In: Haralick RM, Shapiro LG, editors. Addison-Wesley; 1991.
[49] Haralick RM, Shanmugam K, Dinstein I. Textural features for image classification. IEEE Trans Syst Man Cybern – TSMC 1973;3(6):610–21.
[50] Wendling A, Hivet G, Vidal-Salle E, Boisse P. Consistent geometrical modelling of interlock fabrics. Finite Elem Anal Des 2014;90:93–105.
[51] Edelsbrunner H. Geometry and topology for mesh generation. Cambridge University Press; 2001.
[52] Persson P-O, Strang G. A simple mesh generator in MATLAB. SIAM Rev 2004;46(2):329–45.
[53] Parthasarathy VN. A comparison of tetrahedron quality measures. Finite Elem Anal Des 1993;15:255–61.
[54] Lo SH. Optimization of tetrahedral meshes based on element shape measures. Comput Struct 1997;63(5):951–61.
[55] Kwok W, Chen Z. A simple and effective mesh quality metric for hexahedral and wedge elements. IMR 2000:325–33.
[56] Knupp PM. Algebraic mesh quality metrics for unstructured initial Meshes. Finite Elem Anal Des 2003;39:217–41.
[57] Boehler JP. A simple derivation of representations for non-polynomial constitutive equations in some case of anisotropy. J Appl Math Mech 1979;59: 157–67.
[58] Potluri P, Sagar TV. Compaction modelling of textile preforms for composite structures. Compos Struct 2008;86:177–85.